In situ X-ray diffraction study of a TiO2 nanopowder Spark Plasma Sintering under very high pressure

Sandrine Cottrino, Thomas Gaudisson, Stéphane Pailhes, Emanuela Archina Ferrara, S. Mishra, S. Daniele, Mohamed Mézouar, Alain Largeteau, Yann Le Godec, Sylvie Le Floch

In situ X-ray diffraction study of a TiO_2 nanopowder Spark Plasma Sintering under very high pressure

Sandrine Cottrino [a,*], Thomas Gaudisson [b], Stéphane Pailhès [b], Emanuela Archina Ferrara [a], Shashank Mishra [c], Stéphane Daniele [d], Mohamed Mézouar [e], Alain Largeteau [f], Yann Le Godec [g], Sylvie Le Floch [b,*]

[a] *MATEIS, INSA-Université Lyon1-CNRS, UMR 5510, INSA de Lyon, 69621 Villeurbanne, France*
[b] *Institut Lumière Matière, Université Lyon1-CNRS, UMR 5306, Université de Lyon, 69622 Villeurbanne, France*
[c] *IRCELYON, Université Lyon1-CNRS, UMR 5256, 2 Avenue Albert Einstein, 69626 Villeurbanne, France*
[d] *CP2M, Université Lyon 1-CPE Lyon-CNRS, UMR 5128, 43 Bvd du 11 Novembre 1918, 69616 Villeurbanne, France*
[e] *European Synchrotron Radiation Facility, Grenoble F-38043, France*
[f] *CNRS, Bordeaux INP, ICMCB, UMR 5026, University of Bordeaux, F-33600 Pessac, France*
[g] *IMPMC, UMR 7590 CNRS - Sorbonne Université - MNHN, Campus Jussieu, 4 place Jussieu, F-75005 Paris, France*

ARTICLE INFO

Keywords:
Nanopowder TiO_2
In situ X-ray diffraction
High-pressure spark plasma sintering
Grain growth
Activation energy

ABSTRACT

We investigated the effect of very high pressure on the sintering temperature, phase transition and the grain growth during Spark Plasma Sintering (SPS) of a 15 nm TiO_2 nanopowder. Using *in situ* synchrotron X-ray diffraction during sintering at 1.5 and 3.5 GPa, we followed the evolution of the crystalline phases and the crystallite size as a function of temperature. In comparison, in the laboratory, SPS experiments were performed on two original facilities: A Paris-Edinburgh press and a high-pressure module adapted to standard SPS equipment. We studied the effect of the pressure on the sintering in the range 76 MPa to 3.5 GPa. We have shown that highly dense nanostructured ceramics can be prepared under very high pressure at low sintering temperatures. At 1 GPa, we limited the grain growth to an average size of 233 nm by heating at only 560 °C, and achieved a relative density of 98 %.

1. Introduction

Nanocrystalline TiO_2 has attracted increasing interest as a functional ceramic and therefore appropriate sintering mechanisms have been widely studied. The highly active and large surface area induced by nanoscale is a key parameter for catalytic, photocatalytic [1] and gas sensing applications [2]. It has been demonstrated that the high pressure preparation induces an improvement of the photocatalytic activity [3] and that the high pressure TiO_2 phase (columbite) opens new opportunities for photocurrent generation under visible light [4]. Slightly doped TiO_2 ceramics are promising candidates as high temperature thermoelectric devices working in oxidising environments [5] and capacitor - varistor ceramics [6]. The electrical properties of TiO_2 are deeply affected by the microstructure, showing an increase of the conductivity by reducing the grain size [7]. To develop nanoceramics, processes typically start with a nanocrystalline powder that can give a faster densification kinetic with a lower sintering temperature, but on the other hand, leads to a higher grain growth rate. Conventional sintering does not allow the elaboration of dense nanoceramics without the use of grain growth inhibitors. Spark Plasma Sintering (SPS) technique combines uniaxial pressure and high intensity pulsed current. It has been found that this process allows a significant reduction in the densification temperature [8]. Indeed, SPS is one of the techniques among the fast sintering approaches allowing to obtain bulk nanoceramics by tuning the kinetics and the uniaxial pressure to prevent grain coarsening and to favour densification phenomena. Despite its renowned strengths, in many cases, SPS fails to retain nanoscale grain sizes while achieving full densification. In fact, the current SPS technique is limited to a pressure of 150 MPa (or 400 MPa with tungsten carbide (WC) mould). However, it has been shown that very high pressure ($P > 1$ GPa) can significantly lower the powder densification temperature [9]. Therefore, interest in high pressure SPS is growing. By replacing graphite punches and die with silicon carbide in standard SPS device, a pressure of 1 GPa can be achieved [10,11]. To reach higher

* Corresponding authors.
E-mail addresses: sandrine.cottrino@insa-lyon.fr (S. Cottrino), sylvie.le-floch@univ-lyon1.fr (S. Le Floch).

pressures special high pressure cells currently used in high pressure labs have been adapted by coupling pulsed current heating to a belt press (6 GPa-1800 °C) [12] or a toroidal anvil device (8 GPa-1800 °C) [13]. Coupling the very high pressure and SPS techniques, we developed a high pressure SPS (HP-SPS) device (up to 10 GPa) [14] based on a Paris-Edinburgh press. In this report, in complement to our previous study carried out on a 2 mol% Nb-TiO_2 powder [15], the objective is to understand the effect of pressure on pure titanium oxide powder during SPS sintering on densification, phase transition and grain growth phenomena. In order to observe this effect, three experiments were performed at different pressures (76 MPa, 400 MPa, 500 MPa) with the same heating cycle at 700 °C. Then, in order to further investigate the effect of very high pressure, two SPS sintering at 1 GPa were performed, and we followed by *in situ* synchrotron X-ray diffraction the grain growth and the phase transition of a TiO_2 nanopowder during sintering under 1.5 and 3.5 GPa. This type of real-time analysis is not possible on any other SPS device. It is a powerful means to study the mechanisms involved in SPS process and optimise the conditions of material sintering. At the end of the study, a calculation of the activation energies of the sintering and the grain growth is proposed to identify the main densification mechanism [16].

2. Materials and methods

2.1. TiO_2 nano-powder synthesis

The $[Ti(OEt)_4]_3$ (Strem Chemicals, 99.9 %) was distilled prior to use whereas the anhydrous n-pentane, obtained from a solvent purification system (MB SPS-800 from MBRAUN), was stored under argon over 4 Å molecular sieves. In a typical sol–gel synthesis of titania nanoparticles, the solution of $[Ti(OEt)_4]_3$ (26 g, 38 mmol) in 50 mL of n-pentane was added to 450 mL of boiling deionized water containing 3.70 g (11.5 mmol, 0.1 eq/Ti) of tBu_4NBr. After stirring the obtained suspension for 2 h at 100 °C, it was centrifuged to obtain a white solid. The as-prepared precipitate was first washed with deionized water (3 × 80 mL) and then with ethanol (1 × 70 mL). After drying the powder at 80 °C for 12 h, it was calcined at 500 °C for 4 h in air to remove all the organic residues. The obtained powder was crystallised in the anatase phase (JCPDS no. 00-021-1272) with a brookite fraction of 17 %. The average crystallite size, determined by Rietveld refinement, was around 15 nm.

2.2. SPS densification

The titanium dioxide powders were sintered by Spark Plasma Sintering (SPS) HPD 25 (FCT Systeme GmbH, Germany). The sintering temperature was measured using a K-type thermocouple (1 mm diameter) introduced into the die. The pulse pattern consisted of two 10 ms pulses followed by a 5 ms pause period. First of all, the powder was pressurised at the targeted pressure (76 MPa, 400 MPa, 500 MPa and 1 GPa). Depending on the pressure, different types of dies were used. For 76 MPa, we used a usual graphite die [5]. For 400 MPa, a tungsten cemented carbide (WC-Co) die with an inner diameter of 10 mm was used [15]. A silicon carbide die (10 mm diameter) placed in a graphite die [17] allowed to reach 500 MPa. For 1 GPa, a special designed Paris-Edinburgh-SPS high pressure cell (SPS-PE cell) was used [14]. In this case, a pellet (7 mm in diameter and 3 mm thick) of pre-compacted powder (at 370 MPa) is inserted in a graphite tube surrounded by a gasket made of fired pyrophyllite. This assembly is placed between two opposed anvils with a pseudo-conoidal profile which reduces the uniaxial stress (Fig. 1a). The anvils are made of Cobalt-cemented tungsten carbide supported by a steel binding ring. The pressure is generated by applying load on the anvils. The gasket plastically flows and transfers a quasi-hydrostatic pressure to the sample. A thermoplastic PEEK (polyether ether ketone) supporting ring around the gasket enhances the pressurisation efficiency. The calibration of the pressure was previously done following the measurement of the equation of state of NaCl by *in situ* neutron diffraction at ISIS facility [18]. Using a Paris-Edinburgh portable press (Fig. 1c), the pressure on a 7 mm diameter sample can reach 5 GPa for a 700 kN load. As the maximum load applied with the FCT-SPS HPD 25 apparatus is 250 kN, the maximum pressure achieved with the Paris-Edinburgh module mounted in the FCT-SPS HPD 25

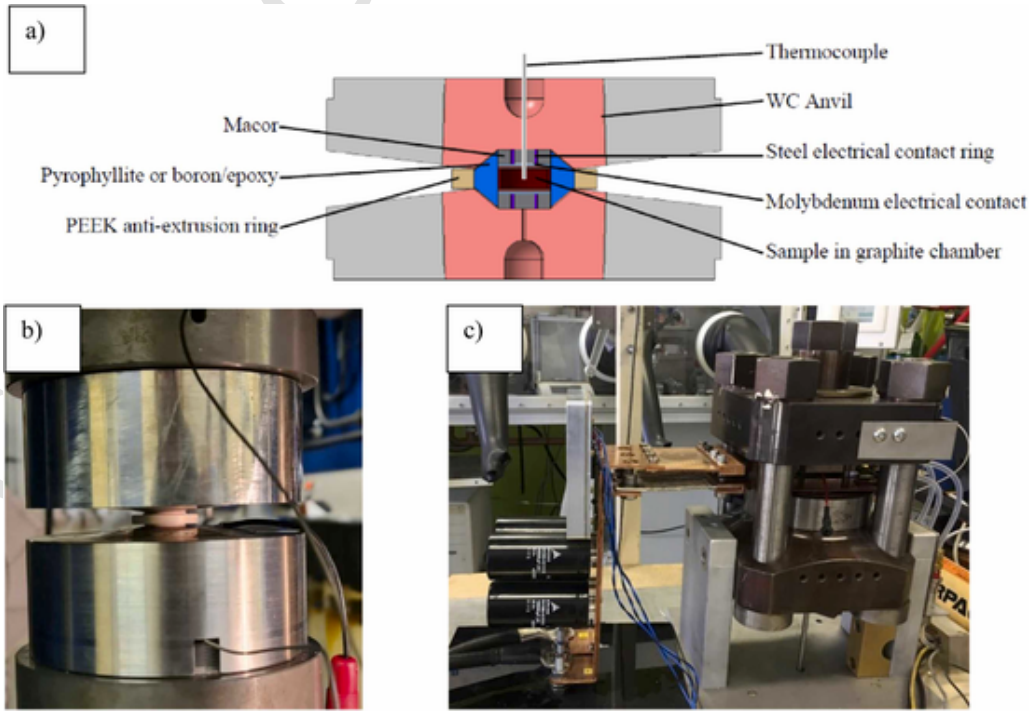

Fig. 1. (a) Section view of the sample cell assembly between two WC anvils (b) The Paris-Edinburgh HP-SPS module mounted in the SPS-HPD 25 (FCT) chamber, working up to 2 GPa (c) The Paris-Edinburgh press coupled with a pulsed current generator, working up to 5 GPa [6].

chamber is 2 GPa (Fig. 1b). The temperature can be measured at the top of the sample with a thermocouple passing through the drilled anvil.

The heating cycle was applied for each experiment with a rate of 100 °C/min and 10 min of dwell time. After the holding time, the heating power was shut off and the pressure released. Three samples were sintered at 700 °C for 76 MPa, 400 MPa and 500 MPa, followed by two others under 76 MPa at 750 °C and 960 °C and two more under 400 MPa at 450 °C and 600 °C. Finally, two samples were sintered at 1 GPa with a temperature of 560 °C and 650 °C.

2.3. In situ synchrotron X-ray diffraction during SPS process

The Paris-Edinburgh press coupled to a pulsed current generator was installed on the ID27 beamline at the European synchrotron radiation facility. Two experiments were performed at 1.5 and 3.5 GPa. During heating to 725 °C with a rate of 8 °C/min, X-ray diffraction patterns of the sample were collected with a rate of one pattern per minute. The X-ray wavelength was fixed to 0.2468 Å. The diffraction patterns were collected in transmission geometry using a MAR345 image plate scanner (X-Ray Research Company GmbH, Norderstedt, Germany) and circularly integrated using FIT2D software [19]. The sample was heated by a low voltage high intensity pulsed current (up to 1000 A/cm^2).

2.4. Characterisation techniques

The density of sintered samples was measured using Archimedes method with distilled water. The values for the relative densities were calculated assuming a theoretical density of 3.89 g cm^{-3} for anatase phase and 4.24 g cm^{-3} for rutile phase.

X-ray powder diffraction (XRD) was used to analyse the crystallographic phase and to evaluate the crystallite size and their microdistortion. A Bruker D8 Advance A25 diffractometer (Cu k_α radiation at 0.154184 nm) equipped with a Ni filter and 1-D fast multistrip detector (LynxEye, 192 channels on 2.95) was used. The diffractograms were collected at 2θ from 20° to 80° for a total acquisition time of 30 min. The data analyses were carried out with DIFFRAC.Eva software to identify the crystallographic phases.

The diffractograms collected on the laboratory and synchrotron X-ray sources were analysed by TOPAS software. In both cases, the instrumental resolution function was fixed from a measurement on a standard. Using the Rietveld deconvolution method, the average lattice distortion and crystallite size were determined from the width of the Gaussian and Lorentzian function, respectively.

Scanning electron microscopy was used to observe the microstructure of the sintered samples. The average grain size for each pellet was obtained by measuring about 150 grains by a line intercept technique using an image analysis software (ImageJ).

3. Results

To clarify the effect of temperature/pressure on densification, phase transition and grain growth, various experiments were conducted and several samples have been elaborated. Their characteristics are listed in Table 1. After sintering, the samples are in the form of 10 mm diameter blue pellets.

3.1. Effect of pressure on densification and transition phase

In order to analyse the effect of pressure on the densification and phase transition, a series of three experiments were performed at the same sintering temperature equals to 700 °C under 76 MPa, 400 MPa and 500 MPa according to the experimental cycle explained in the 2.2 part. It can be observed on the XRD profiles of the 3 sintered samples that no brookite fraction remains and that the anatase to rutile phase transition occurred at a temperature lower than 700 °C for the samples sintered at 400 and 500 MPa. Indeed, at 700 °C-76 MPa the pellet is approximately half composed of the rutile phase, whereas at higher pressure values, the transition is completed (Fig. 2). The anatase to rutile phase transition usually occurs within 600–850 °C with a volume reduction of 9 % [20,21]. In fact, anatase is the most stable phase at nanoscale whereas rutile is the thermodynamically stable phase in coarse grains [22]. Therefore, pressure-induced nanoanatase transformation may follow different pathways depending on the surface chemistry and size of the nanoparticles [23,24]. The application of pressure during SPS sintering is known to induce the phase transition anatase-rutile at lower temperatures [15].

Sintering steps of the four samples (700 °C-76 MPa, 400 MPa, 500 MPa and 650 °C-1 GPa) can be evidenced thanks to the piston displacement (Fig. 3a) and its rate (Fig. 3b) as function of temperature. In Fig. 3a, we can observe that the densification starts at lower temperature when high pressure is applied. Fig. 3b allows to evidence the different densification steps. At low pressure (76 MPa), individual phase transition events were not evident. However, at the higher pressures of 400 MPa, 500 MPa and 1 GPa we can distinguish different peaks corresponding to densification of the anatase phase, then phase transition

Table 1
Characteristics of all samples produced in this study. Each pellet is sintered with 1 g of TiO_2 powder, except samples at 450 °C and 600 °C under 400 MPa for which 0.7 g of powder was used and for two samples under 1 GPa for which 0.5 g of powder was used.

Pellets	Phases (A + R = 100 %)	Relative density (%)	Mean grain size (nm)	Crystallite size (nm)		D10 (nm)	D50 (nm)	D90 (nm)
				Anatase	Rutile			
700 °C-76 MPa	65.5 % R	90.1	144	62	133	80	130	220
750 °C-76 MPa	98.4 % R	91.3	227	/	80	150	220	320
960 °C-76 MPa	100 % R	99.2	530	/	109	340	510	700
450 °C-400 MPa	80 % R	96.9	225	71.2	201	140	220	310
600 °C-400 MPa	100 % R	98.4	315	/	127	200	280	350
700 °C-400 MPa	100 % R	98.5	383	/	131	180	350	450
800 °C-400 MPa	100 % R	99.1	435	/	193	240	400	530
700 °C-500 MPa	100 % R	98.5	333	/	225	210	310	430
560 °C-1 GPa (16 °C/min)	100 % R	98.0	233	/	163	130	230	370
650 °C-1 GPa (16 °C/min)	100 % R	98.1	266	/	176	140	260	440
530 °C-1 GPa-10 min (70 °C/min)	100 % R	95.0	248	/	163	150	250	350
725 °C-1.5 GPa/5 min (8 °C/min)	100 % R	/	700	/	312	390	640	1140
725 °C-3.5 GPa/2 min (8 °C/min)	100 % R	/	430	/	166	275	420	670

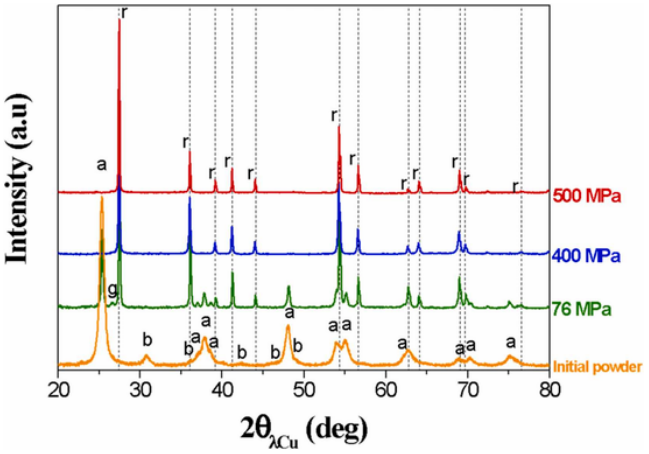

Fig. 2. XRD profiles for the initial powder calcined at 500 °C/4 h, pellets sintered by SPS at 700 °C under 76 MPa, 400 MPa and 500 MPa. Peaks are identified as anatase (a), brookite (b), rutile (r) and graphite peaks (g). The latter refers to graphite residue on the sample surface originating from the graphite foil placed between the die and TiO_2 powder during sintering.

and finally the densification of the rutile phase [15]. In fact, at 76 MPa-700 °C it is evident that densification of the anatase phase occurs progressively until a final phase transition occurs at 700 °C (to retain 58 % Rutile phase in the final product). At 400 MPa, the phase transition occurs around 430 °C (as evidenced from the XRD analysis on the pellet sintered at 450 °C-400 MPa giving 80% rutile phase and 20 % anatase phase). Hence, the first peak represents the anatase densification and at the end the phase transition. The second peak can be assigned to the rutile densification. At 500 MPa, three steps can be observed which could correspond to anatase densification (peak 1 in Fig. 3b), phase transition (peak 2 in Fig. 3b) and rutile densification (peak 3 in Fig. 3b). A sample sintered at 400 °C under 500 MPa contains 20 % rutile, 65 % anatase and 15 % brookite. This confirms the transition anatase-rutile at 400 °C under 500 MPa. But we notice that the brookite phase is still present at this stage of the densification, which was not the case at lower pressure. The same three stages of densification, shifted to lower temperatures, are clearly observed at 1 GPa as three well-defined peaks in the displacement rate (Fig. 3b). This means that densification and phase transition are faster at high pressure and occur in distinct narrower distinct temperature ranges.

As seen in previous work [15], the rutile phase has a higher density (4.24 g/cm^3 *versus* 3.89 g/cm^3 to the anatase phase), involving a volume reduction of 9 % at the transition anatase to rutile. A more compact granular arrangement with more constrained grains, can favour the nucleation of rutile that can occur either at grain surface or in the bulk. This may explain the shift of the phase transition towards lower temperatures [9]. Fig. 3c shows the temperature evolution of the two densification stages and the transition observed in Fig. 3b as a function of pressure. Up to 500 MPa, the effect of pressure is significant. The anatase densification, phase transition and rutile densification temperatures are lowered by 240 °C, 300 °C and 400 °C respectively. No further significant shift is observed above 500 MPa.

We may point out that the density of the green pellet after the application of the pressure and before heating varies from 29 % under 76 MPa to 64.4 % under 1 GPa (Fig. 12c). Regardless of the sintering technique used, the density of the green compact has an impact on grain growth and densification. The finer the nanopowders, less compactable they are. This may be due to the ability of ultrafine powders to agglomerate due to Van der Waals attraction [25]. We evaluated the relative density of our compacted powder under pressure at room temperature using a WC matrix and a Zwick testing machine. The plot of the relative density of the green compact as a function of the logarithm of the pressure (Fig. 4) shows two linear regimes with a intercept point at P_b equal to 330 MPa. This is consistent with the P_b determined equal

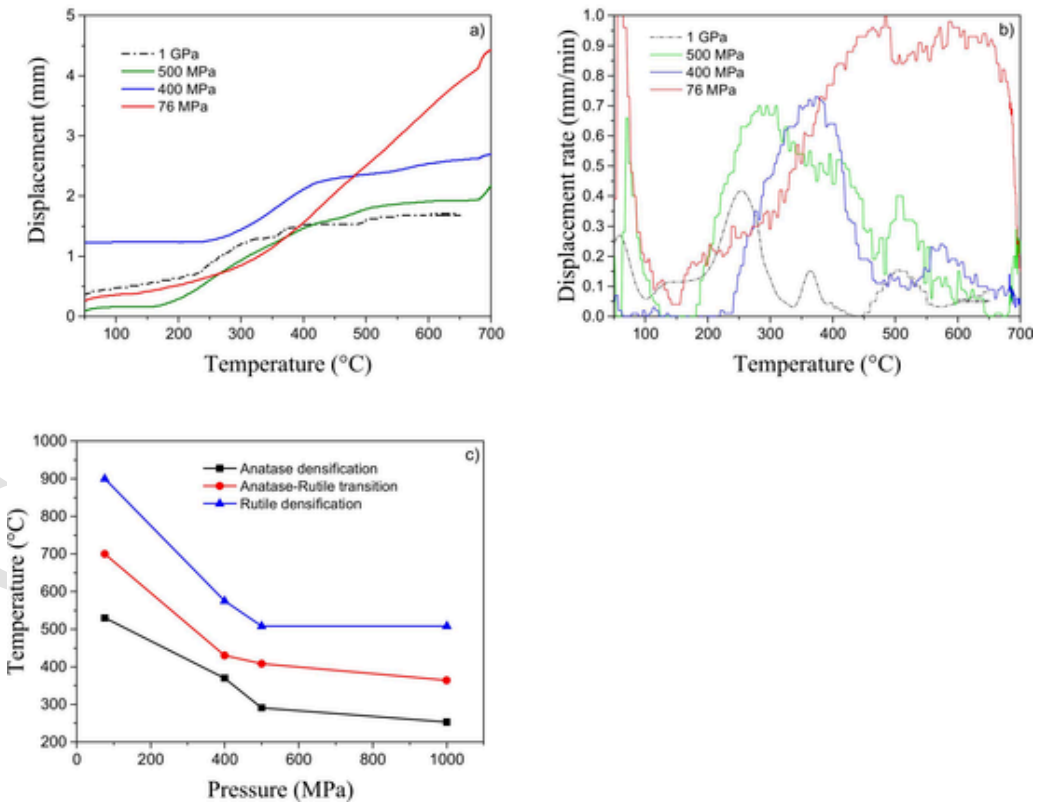

Fig. 3. a) Dilatometric curves registered at 76 MPa, 400 MPa, 500 MPa up to at 700 °C with 100 °C/min heating rate and under 1 GPa up to 650 °C with 16°/min heating rate; b) Corresponding displacement rates; c) Temperature evolution of the 3 mechanisms observed during densification as a function of pressure.

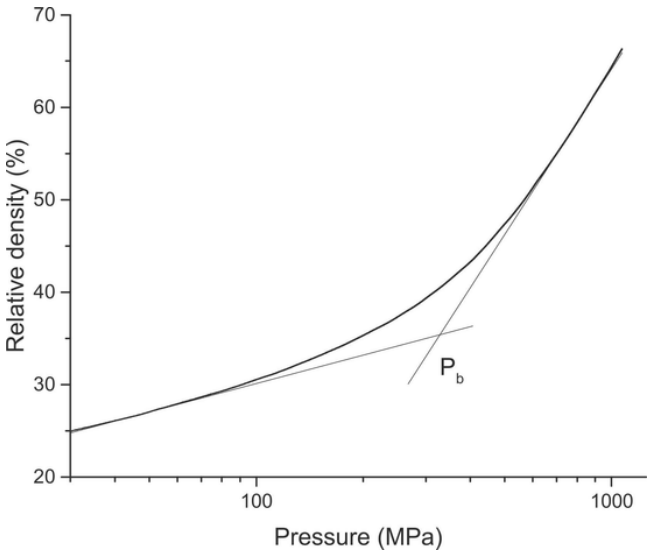

Fig. 4. Green density plotted *versus* logarithm of applied pressure.

to 380 MPa by Alvarez-Roca et al. [25] for a 10 nm anatase powder. According to their study with a compaction pressure above P_b, the agglomerates are fragmented, while below P_b they are only rearranged. We can identify two mechanisms of particles rearrangements during the compaction: inter-agglomerates below P_b and intra-agglomerate above P_b. This leads to higher relative density of the green compact when a pressure above 330 MPa is applied. This partially explains the difference of the densification pathway at 76 MPa as compared to the sintering at pressures higher than 330 MPa.

3.2. *In situ observation during sintering at very high pressure*

We performed two *in situ* synchrotron X-ray experiments at 1.5 and 3.5 GPa. The series of diffractograms recorded during heating is quite similar for both experiments. These diffractograms are shown for the experiment at 3.5 GPa in Fig. 5. *In situ* XRD highlights the anatase-rutile transition at 315 and 295 °C for the experiments at 1.5 and 3.5 GPa respectively. In both experiments the brookite phase remains until this transition and disappeared with the anatase phase.

Using TOPAS software, we evaluated the evolution of the crystallite size for anatase and rutile during heating (Fig. 6a and c). Before the anatase-rutile transition, at around 300 °C, the anatase crystallite size increases from 15 to 25 nm. Then, the conversion anatase to rutile induces a jump in the crystallite size to 40 nm. The nucleation of the rutile occurs at the interface of the anatase grains and the rutile phase grows to the inside of the grains. Therefore, the formation of rutile grains mainly occurs by the merger of two anatase particles leading to a rapid grain growth at the phase transition [26]. For crystallite size higher than 50 nm, TOPAS failed in the evaluation of the crystallite size with the synchrotron instrumental resolution function. The calculated values reach an upper limit that does not correspond to the reality. The recovered samples were analysed on the laboratory diffractometer. In that case, TOPAS evaluates the rutile crystallite size at 312 nm and 166 nm for sintering at 1.5 and 3.5 GPa, respectively. These values are reported in Figs. 6a and 6c. The growth of rutile crystallites is lower at 3.5 GPa. The crystallites microdistortions given by TOPAS are shown in Figs. 6b and 6d. The microdistortions in anatase crystallites are 3 times higher at 3.5 GPa than at 1.5 GPa. They start to relax at 200 °C. The relaxation is complete after the phase transition.

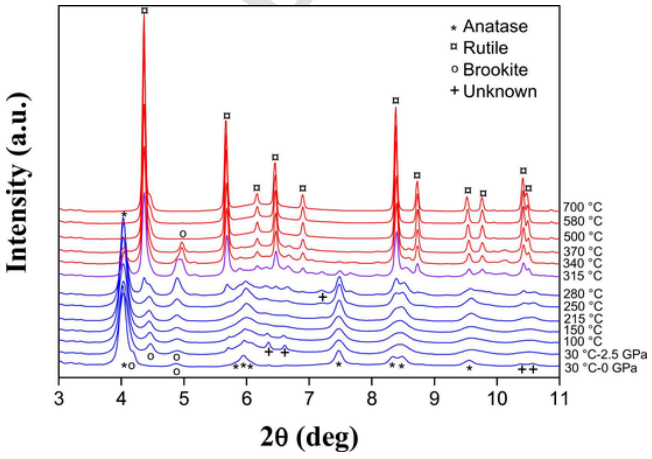

Fig. 5. *In situ* X ray diffractograms recorded during sintering at 3.5 GPa (λ = 0.2468 Å).

3.3. *Effect of pressure on grain size*

In order to measure the grain size, SEM observation was carried out on the samples sintered at 700 °C with different pressures (76, 400, 500 MPa) and 650 °C-1 GPa. SEM images are shown in Fig. 7a–d. At 76 MPa-700 °C, the shape of the grains and the overall microstructure show that the pellet is not yet well densified compared to the others. Indeed, this sample remains mostly crystallised in anatase and its relative density (d_r) is only 90 %. At the same temperature but at higher pressure, the pellets are well densified and the grains have a characteristic polygonal shape. Indeed, the relative density is approximately 98 % for these pellets. At this level of density (last stage of densification) a coarsening of the grains occurs resulting in a heterogeneous microstructure. Nevertheless, the average size of the grains decreases with the pressure for the same sample density (383 nm, 333 nm and 266 nm respectively for 400 MPa, 500 MPa and 1 GPa). The SEM image at 1 GPa clearly shows the presence of two populations of grains.

If we observe the microstructure on SEM images (Fig. 8) of samples sintered by SPS at 1.5 GPa and 3.5 GPa during the synchrotron experiment, a finer microstructure is also observed at 3.5 GPa as compared to 1.5 GPa. Grain size values of samples sintered at synchrotron cannot be compared with the other ones as the heating rate was twelve times slower.

To quantify the broadening of grain size distributions, SEM images are analysed. Figs. 9 and 10, show the grain size distribution of 6 samples sintered at different pressures. If we do not consider the sample treated at 700 °C under 76 MPa, as it is not well-sintered (relative density equal to 90 %), the mean size decreases with increasing pressure. Small grain population increases with the pressure and the coarse grain population decreases. For both samples sintered at 1.5 GPa and 3.5 GPa, during the synchrotron experiment, the average grain size is larger due to a slower heating rate (8 °C/min), but the evolution between 1.5 GPa and 3.5 GPa is similar to the samples set 400 MPa to 1 GPa.

To clearly underline the fact that the application of strong pressure during sintering activates densification mechanism at lower temperature and allows to obtain a same densification state of the pellets with a finer microstructure, the evolution of grain size, crystallite size and density as function of pressure sintering are represented in Fig. 11. At 700 °C-76 MPa, the pellet density is only around 90 %. For 700 °C-400 MPa, the density pellet reaches 98.5 %. For 700 °C-500 MPa or 650 °C-1 GPa, the density level is similar but the grain size is smaller. It can be observed that the size of crystallite is lower than grain size. As shown in our previous study [15], under high pressure the high stress level on the grains leads to their fracture. After the phase transition, different crystal domains appear inside the grains.

The evolution of grain size, crystallite size and relative density is plotted as function of temperature for same pressures (76 MPa, 400 MPa and 1 GPa) in Fig. 12. If we observe the evolution of the den-

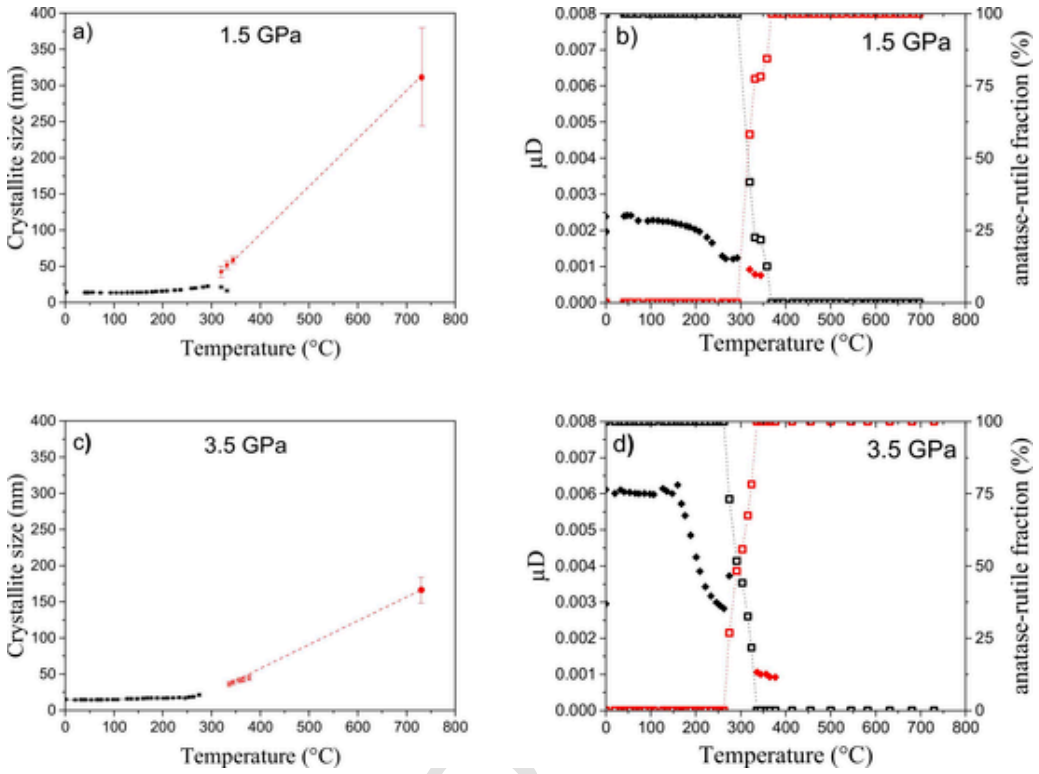

Fig. 6. a) and c) Crystallite sizes extracted from the diffraction patterns recorded during *in situ* SPS experiments at 1.5 and 3.5 GPa, respectively. Values corresponding to 740 °C were obtained from *ex situ* measurements on the recovered samples; b) and d) Crystallographic microdistortion (filled diamonds) and fraction of phases (open squares) evolution during sintering at 1.5 and 3.5 GPa. Black and red marks referred to the anatase and rutile phases, respectively.

sity (Fig. 12a), it appears that under high pressure the densification is faster and a relative density higher than 95 % is reached as low as 400 °C. As shown in Fig. 4, the green density of the pellet is improved when the applied pressure exceeds 330 MPa. Above this pressure the agglomerates are broken allowing the rearrangement of the particles at room temperature. If we observe grain size, it appears that at low pressure (76 MPa), higher temperatures are needed to reach a high level of densification (> 98 %) and thus the microstructure is coarser. Indeed, at high temperature, mechanism of grain boundary diffusion is accelerated (high thermal energy) and thus leads to grain growth. In Fig. 12b, it appears that the crystallite size is lower than grain size, as previously observed for the samples sintered at 700 °C at different pressures. A marked increase of the crystallite size occurs during the transition phase. As we observed with *in situ* X-ray diffraction, the rutile crystallites formed are two times larger than the remaining anatase crystallites. But just after the transition a remarkable decrease of the rutile crystallite size is observed. The same evolution of rutile crystallite size is observed by Maglia et al. [27]. In fact, the final grain size of rutile is controlled by the competition between two rutile formation phenomena: nucleation in anatase surface and growth in bulk anatase grain [28]. Nucleation within anatase bulk grain requires a higher activation energy and thus occurs at higher temperature. Thus, the first nucleation process that occurs, is around the grain boundaries. Boundary nucleation gives rise to larger rutile grains. In fact, one or more anatase grains are transformed in single rutile particle. This explain that the first rutile crystallites formed at the beginning of the transition are larger as compared to those formed in the second part of the transition. Regarding the grain size (Fig. 12a), it increases steadily with increasing temperature after the phase transition with a lower growth rate as the pressure increases. This is explained by Liao et al. with a decrease of the diffusivity when very high pressure (at least 1 GPa) is applied leading to a decrease of the growth rate [28,29].

3.4. Apparent activation energy of grain growth

We observed in this study like in previous ones [15,30,31] that applied high pressure during the sintering decreases the sintering temperature by activating the densification and the grain growth mechanisms earlier and faster. To quantify the effect of pressure in terms of kinetic, the Arrhenius equation is used to calculate the apparent activation energy of these phenomena. Activation energy is the minimum amount of energy required to initiate a chemical reaction. The lower this energy is, the stronger the driving force of the reaction is. Depending on the mechanism studied, densification or grain growth, different values of activation energy have been calculated. Indeed, Arrhenius law establishes the dependence of the rate of a chemical reaction on temperature. Depending on whether we are interested in the grain growth rate or the densification rate, we will obtain activation energies specific to each mechanism.

The latter stage grain growth, when the relative density exceeds 90 %, can be analysed using the conventional power law of the grain growth [32–34]:

$$\log\left(\frac{G^n}{t}\right) = \log\left(K_0\right) - 0.434 * \frac{Q}{R} * \left(\frac{1}{T}\right)$$

with G the grain size value after sintering (m), t the dwell time (h), K_0 a constant, R the ideal gas constant (J mol^{-1} K^{-1}), T the sintering temperature (K) and Q the activation energy (kJ/mol). The exponent, n, varies depending on the mechanisms [16]. Considering that the predominant mechanism is grain boundary controlled, we used n = 2. Thus, knowing the grain size and the sintering temperature, the apparent activation energy can be calculated by linear fitting (Fig. 13). In this study, activation energies at 76 MPa, 400 MPa and 1 GPa have been estimated.

First, it is important to state that the main grain growth occurs at the final stage of sintering, when a density of at least 90 % is reached [35].

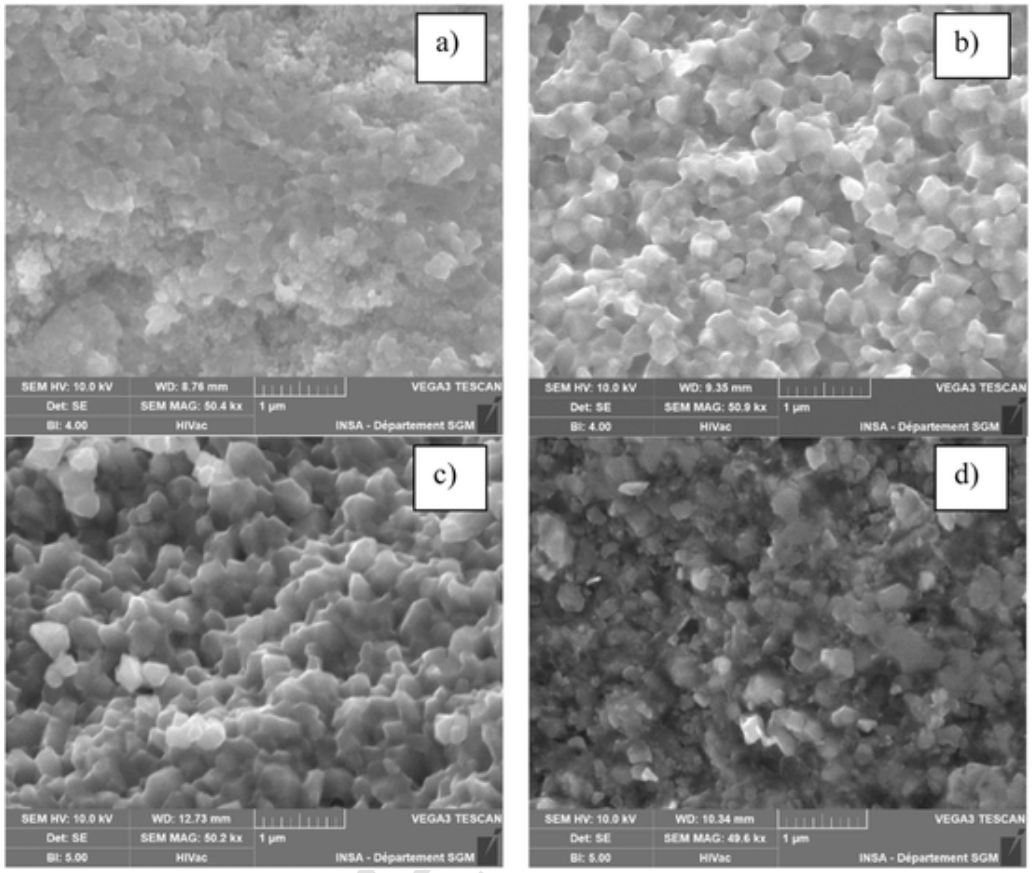

Fig. 7. SEM images of sintered powder at 700 °C under 76 MPa - d_r 90.1 % (a), 400 MPa - d_r 98.5 % (b) and 500 MPa - d_r 98.5 % (c) at 650 °C under 1 GPa - d_r 98.1 % (d).

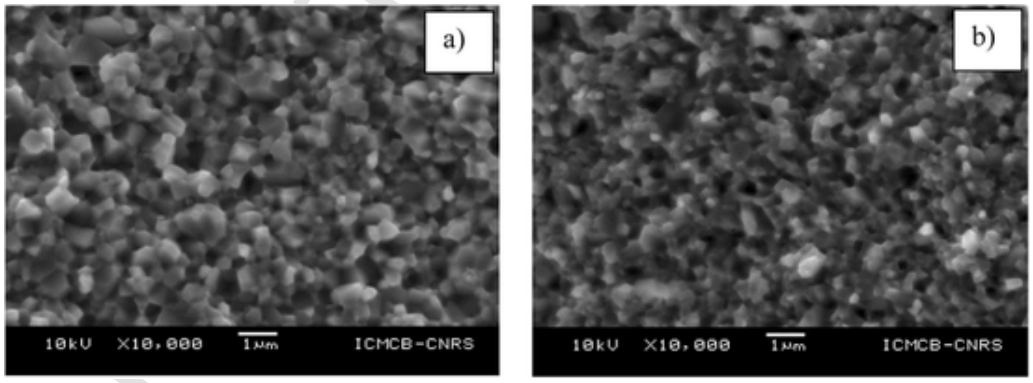

Fig. 8. SEM images of sintered powder at 725 °C under 1.5 GPa (a) and 3.5 GPa (b).

Second, the transition from the metastable anatase phase to the stable rutile phase is accompanied by considerable grain growth [20]. We estimated the activation energy of the grain growth of rutile during the final sintering stage when most of the grains are converted in rutile. At low pressure sintering, an activation energy of 229 kJ/mol has been estimated for rutile grain growth in the temperature range 700–960 °C. In literature, in the case of a conventional sintering, a value of 360 kJ/mol, consistent with our result, has been evaluated, in the range 1000–1250 °C, for grain growth of a barium titanate nanopowder, with a bimodal distribution (200 and 80 nm) [33]. Under low pressure (76 MPa), sintering phenomena are slow and extended over a large temperature range and phase transition is only fully achieved for temperature higher than 700 °C. Furthermore, the final step of densification occurs above 700 °C. In this temperature range, ionic diffusion coefficients are higher and grain coarsening is facilitated. In contrast, the activation energies calculated at 400 MPa and 1 GPa are significantly lower. From the definition of Arrhenius law, this means that the grain growth occurs at lower temperature. This is shown in Fig. 12 where it can be seen that grain growth of rutile phase starts around 450 °C compared to 700 °C at 76 MPa.

3.5. Apparent activation energy of sintering

To compare the SPS sintering behaviour of nanopowder under different pressures, we used the displacement of punch to obtain a dilatometric curve. Dilatometric analysis allows to estimate the densification energy activation thanks to the so-called constant rate of heating method (CRH) [36]. A prerequisite for calculating the apparent activation energy is to be sure that the sintering mechanism is solid phase sintering [37]. The CHR method, as explained in Weibel's study, is useful

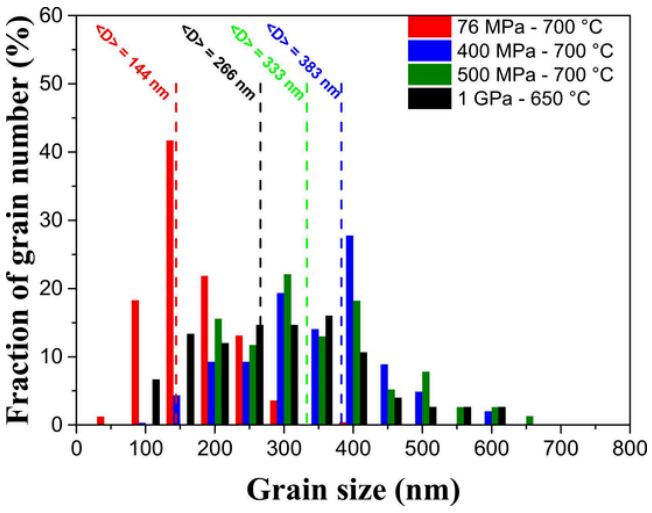

Fig. 9. Grain size distribution of pellets sintered at 700 °C for 10 min under different pressures. Grain size is the grain diameter measured on the SEM images (50–175 values per sample). The data are discretized in twelve 50 nm width intervals.

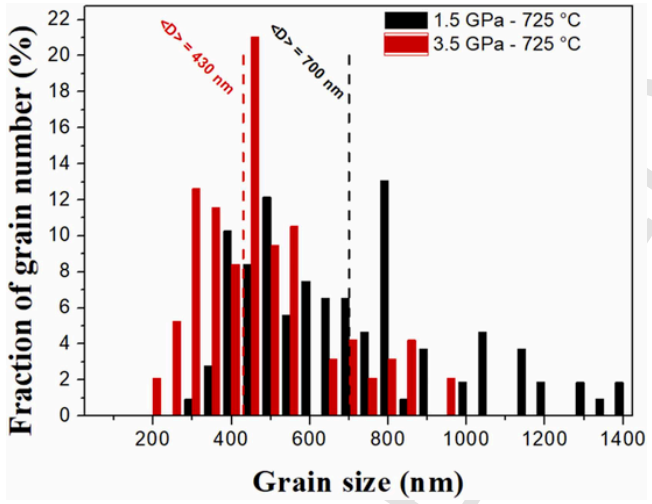

Fig. 10. Grain size distribution of pellets sintered at 725 °C under 1.5 and 3.5 GPa. Grain size is the grain diameter measured on the SEM images (50–175 values per sample). The data are discretized in twelve 50 nm width intervals.

only during the intermediate stage of sintering, when open porosity is still present (relative density < 90 %). The following expression, derived from Arrhenius law, considers that the predominant mechanism is grain boundary diffusion.

$$\log\left(\frac{\Delta L}{Li}T^{1/3}\right) = \frac{1}{3}\log\left(K_0\right) - \frac{Q}{3R} * \left(\frac{1}{T}\right)$$

With

$$K_0 = \frac{2.14\gamma\Omega RD_{0,GB}}{kr^4cQ}$$

Where γ is the surface energy, Ω the free volume of grain boundary, R the ideal gas constant, $D_{0,GB}$ the diffusion coefficient of grain boundary, r the particle radius and c the constant heating rate.

Like Weibel et al. [36], considering the negligible influence of temperature in the logarithmic term, we determined the effective activation energy of densification process from a simple plot of $\log\left(\frac{\Delta L}{Li.T}\right)$ *versus* $\frac{1}{T}$ (Fig. 13). Effective activation energies determined by CRH method

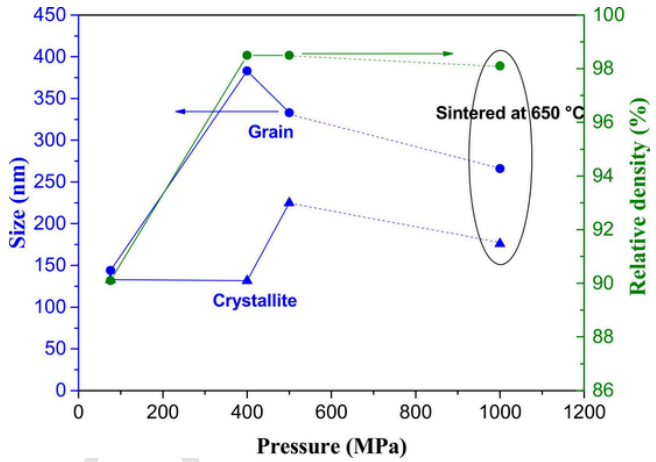

Fig. 11. Evolution of grain size (blue dots), crystallite size (blue triangles) and relative density (green dots) as function of pressure at 700 °C and 650 °C.

for samples sintered under 76 MPa and 400 MPa are presented in Fig. 14. Different slopes are observed for both experiments as function of temperature showing an impact of pressure on densification process. For each pressure, different densification mechanisms take place during heating. The values of activation energy calculated here are close to the literature. Weibel et al. [36] find values of 0.39 eV (37.5 kJ/mol) for a similar nanopowder (12 nm) sintered under pressure (125–600 MPa). In contrast to Weibel et al., we observe different stages of densification in the ranges 200–400 °C and 200–700 °C for a sintering under 76 MPa and 400 MPa, respectively. At very low temperature (< 300 °C), densification is only due to an increase in compactness through the arrangement of the grains and perhaps plastic deformation, as reported for nanocrystalline particles under very high pressure above 1 GPa [36, 38–40]. Higher pressure implies greater compactness and thus a lower activation energy of densification (Ea_1). Above 300 °C, diffusion mechanisms became predominant and the effective activation energy increases (Ea_2). The activation energy, Ea_2, at 400 MPa (23.4 kJ/mol) is significantly lower than at 76 MPa (38.5 kJ/mol). This reflects a facilitated mass transfer phenomenon during the sintering of highly constrained particles.

At 76 MPa and 400 MPa, at the phase transition temperatures respectively, 700 °C and 400 °C (Fig. 14), an inflection of the curves is observed. This densification stage corresponds to the volume contraction of 9 % induced by the phase transition. The corresponding activation energy is lower at 400 MPa (Ea_3 = 7.2 kJ/mol) than at 76 MPa (Ea_4 = 15.8 kJ/mol). This can be explained because pressure promotes the anatase-rutile transition. A 44 % reduction in the energy barrier has been assessed at 1.5 GPa [29].

4. Discussion

The application of high pressures during the sintering of nanopowders has an important impact on the phenomena of densification (rate, activation energy), phase transition and grain growth. In order to improve the electrical, thermoelectric or mechanical properties of a material, it is necessary to have a dense material with a fine microstructure and therefore to minimise grain growth. The difficulty is that densification and grain growth are concomitant processes. Different steps occur during sintering. At low temperature, a slight coarsening of the grain takes place at the same time as the formation of the first sintering necks, then very quickly the densification mechanisms become preponderant with increasing temperature. At high density (> 90 %), the grain coarsening mechanisms become dominant.

When a pressure is applied during a sintering treatment, kinetic of the different processes is modified. Indeed, a maximum densification rate is observed at 250 °C under 1 GPa against 500 °C under 76 MPa

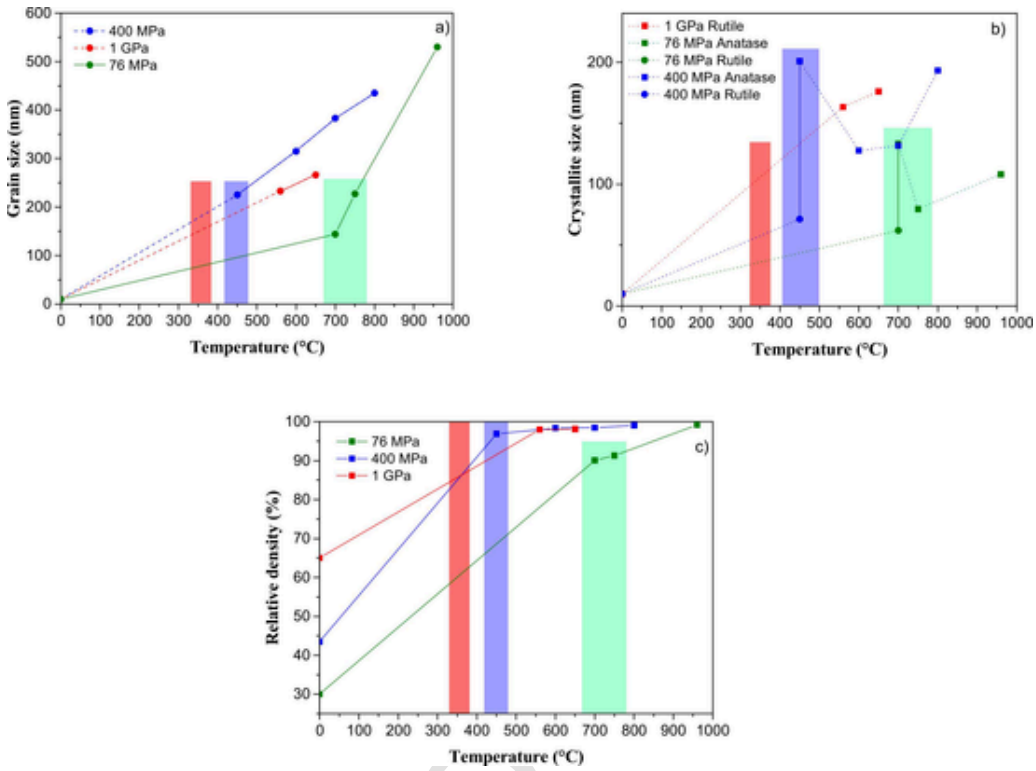

Fig. 12. Evolution of grain size, crystallite size and relative density as a function of the sintering temperature at three constant pressures: 76 MPa, 400 MPa and 1 GPa. For each pressure, the anatase-rutile transition temperature range is represented by a coloured area.

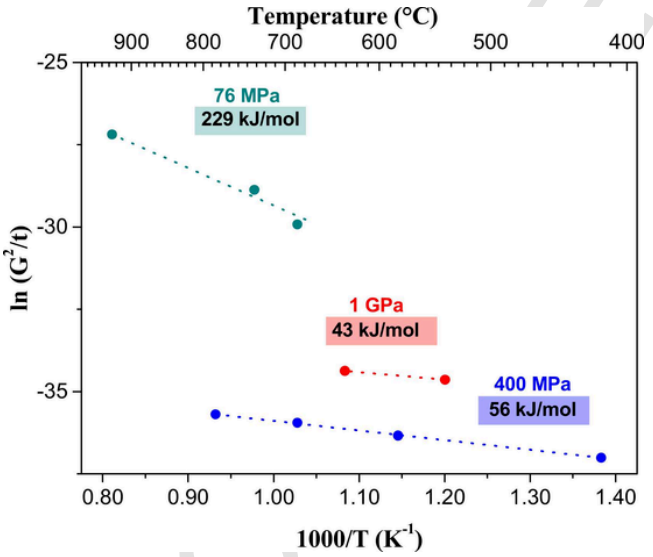

Fig. 13. Arrhenius equation linear fitting diagram for sintered pellets with pure TiO_2 powder at 76 MPa (a), 400 MPa (b) and 1 GPa (c).

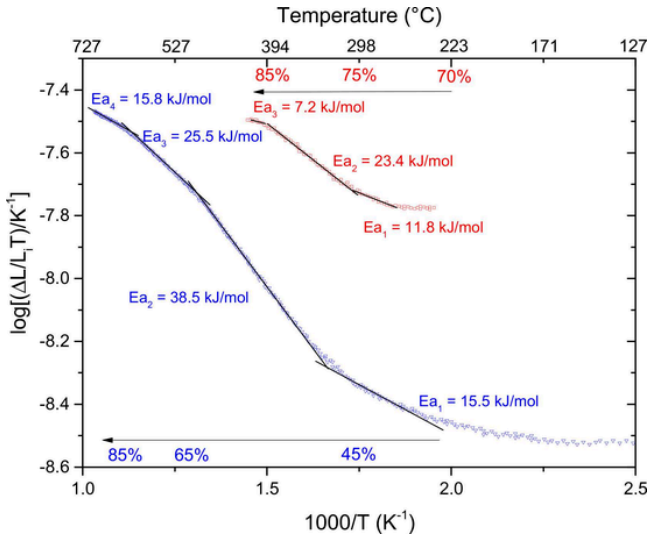

Fig. 14. Activation energies determined by CRH method for sintering at 76 MPa (blue), 400 MPa (red). Relative densities of the samples are indicated in the corresponding temperature ranges.

(Fig. 3). It has been shown that at pressure above 1 GPa, it is possible to densify (d_r 95 %) a nanoanatase powder at low temperatures (400 °C) [9]. To be efficient, the sintering pressure has to be greater than the internal stress of the nanoparticles. For a nanopowder with a crystallite size of 15 nm and thus a radius pore of 6 nm, the calculated internal stress is around 150 MPa [36]. So if the applied pressure is significantly greater than the internal stress of nanoparticles it is possible to densify at lower temperature by superplastic deformation [40,41]. Furthermore, the application of high pressure at room temperature improves the packing density of the green compact by the fragmentation of agglomerates (nanoparticles have a strong tendency to agglomeration due to very high Van der Waals forces). With the pressure increase (above 330 MPa), these agglomerates are broken allowing the rearrangement of the nanoparticles. Green compact relative density reaches 64 % at 1 GPa compared to less than 30 % at 76 MPa. Thus, for pressures above 330 MPa, particles are reorganised in the compact and perhaps plastically deformed for pressure above 1 GPa [36,38,39] allowing to start the thermal sintering from a quite high relative density. This impacts drastically the early sintering stages.

Using *in situ* XRD at 1.5 GPa and 3.5 GPa, no significant crystallite growth is observed at low temperature before the phase transition. During the transition an important grain coarsening occurs explained by the coalescence of anatase crystallites to form rutile crystallites.

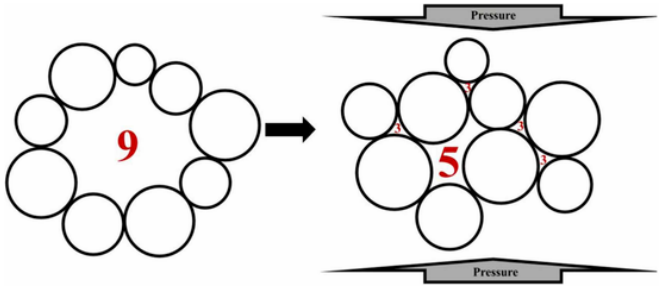

Fig. 15. Illustration of the decrease in pore coordination numbers (indicated in red) due to pore collapse under pressure.

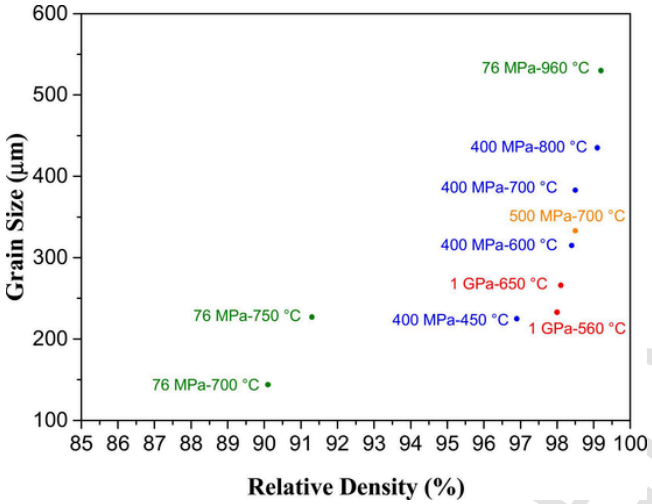

Fig. 16. Grain size *versus* relative density for all samples sintered at different pressures, ranging from 76 MPa to 1 GPa.

The phase transition has been shifted to lower temperature as observed in Figs. 2 and 3. Under high pressure grains are highly constrained. To release these stresses, the nanoparticles undergo structure change from the anatase form to the denser rutile form leading to a 9 % volume decrease. This relaxation during the transition phase is observed in Figs. 6b and 6d. The applied high pressure results in an increased nucleation rate of the rutile phase [28].

If we compare two samples with approximately the same conversion state (80 % rutile at 450 °C-400 MPa and 98 % rutile at 750 °C-76 MPa), the grain size is similar (225 nm) whereas the density is higher at 450 °C-400 MPa. To obtain the same level of density at 76 MPa, it is necessary to heat above 700 °C. At these temperatures, grain coarsening mechanisms become progressively dominant (grain boundary diffusion) over densification mechanisms, and titania is known to possess a high diffusion coefficient for oxygen ions above 500 °C [20]. At 76 MPa, we obtain density superior to 98 % at temperature above 900 °C but with a grain size over 500 nm. In comparison, high pressure sintering produces samples with densities greater than 98 % but at temperatures equal or lower than 700 °C and therefore with grain sizes of 300 nm or even smaller.

As mentioned previously, at low temperature and very high pressure, nanoparticles densification occurs first by a granular rearrangement and then by superplastic deformation that allows to decrease the pore size. This configuration favours densification diffusion phenomena. As described in Section 3.1, at high pressure (400 MPa) activation energy are lower than at 76 MPa. At very low temperature (Ea_1), the densification can be explained by nanoparticles rearrangement and sliding and plastic deformation. Above 300 °C (Ea_2) mass transfer mechanism are facilitated and accelerated. During the initial stage of sintering, surface diffusion and evaporation-condensation together contribute to the formation of necks. [42]. The evaporation-condensation mass transfer mechanism is governed by vapour pressures due to the radii of curvature of particle surface and neck. The gap between the particles is formed by a positive radius of curvature (surface) and negative radius of curvature (neck) at the junction of the particles. The mass transfer takes place from the concave surface to convex surface (sintering neck) by evaporation. The sintering neck is gradually filled while grains grow more or less quickly depending on their initial size [33].

Concerning the microstructure, we have clearly observed that for samples with the same density, the more the applied stress increases, the more the average grain size decreases. Therefore, the grain growth rate decreases with the increase of applied pressure. How can we explain that densifying mass transfer are favoured at high pressure? More the pressure increases, more the granular arrangement is constrained. The particles slide, turn and under very high pressures are plastically deformed (especially for nanometric particles). Deformation may increase the radii of curvature facilitating mass transfer. This may contribute to the activation of densification phenomena at lower temperatures during the high pressure sintering process. During the first stage of densification, pore shrinkage is a predominant phenomenon. Based on Kellett and Lange's model, a porosity is filled only if the pore coordination number (N) is smaller than a critical coordination number (Nc) which depends of particles size and thus dihedral angle[16]. The pore coordination number (N) is the number of particles surrounding a pore (Fig. 15). While $N > Nc$, the pore is stable. When $N < Nc$, the pore is unstable and will shrink. In conventional sintering, grain coarsening reduces N, allowing sintering and densification to continue. But different mechanisms can reduce N. Under high pressure, the pores can collapse and divide in smaller pores with $N < Nc$ (Fig. 15) [43]. N decreases with pressure, which favours the densification mechanisms over those of grain growth.

Under high pressure, a specific grain growth mechanism appears, the grain boundaries sliding (GBS) [31,44]. Under high stress the grains slide, rotate until align their atomic planes resulting in grain growth by grain coalescence. This grain growth mechanism needs less energy and occurs at lower temperature. Therefore, high pressure sintering must be performed at the lowest possible temperature to achieve full densification while minimising grain growth. Our portable HP-SPS device for *in situ* analysis is a powerful tool for optimising pressure, temperature and heating rate to achieve dense nanoceramics. Then, larger products can be obtained in a larger volume high-pressure device associated with a pulsed electric generator [45]. We have shown that HP-SPS is effective in obtaining a finer microstructure in dense ceramics. All samples are plotted in the same graph of grain size *versus* density (Fig. 16). It is clear that the samples sintered at 1 GPa have the finest grain size with a density of over 98 %.

5. Conclusion

High pressure, low temperature SPS sintering of TiO_2 nanopowder was successfully carried out in order to obtain ceramics with finer microstructure and high density. Application of very high pressure on the green pellet allows to highly increase its compactness, by agglomerates organisation under 330 MPa and then fragmentation with intra-agglomerates grain rearrangement at higher pressure. High initial packing density leads to efficient densification phenomena at low temperature. Strongly constrained system promotes a phase transition at lower temperature. Microdistortion are released thanks to phase transition. Very high pressure, higher than 400 MPa, has also an important effect on grain growth. The kinetics are remarkably slowed down. On the final densification step, after the phase transition, very high pressure stabilises finer microstructures. Effect of high pressure on kinetics phenomena has been confirmed by activation energy calculations. Activation energy of sintering decreases with the pressure, confirming the lowering of the sintering temperatures.

Funding

The authors thank CNRS Prématuration Program 2019 and the institute of chemistry of Lyon university (ICL) for funding this study.

Declaration of Competing Interest

The authors declare that they have no known competing financial interests or personal relationships that could have appeared to influence the work reported in this paper.

Acknowledgements

We would like to thank Matthieu Mercury, Clément Albin and Jean-Michel Combes (ILM) for their help in the HP-SPS device. We thank Laurent Gremillard (MATEIS) for his assistance in using TOPAS. HP-SPS experiments were performed at the MATEIS-SPS platform and the PLECE-ILMTech platform.

References

[1] B. Levy, Photochemistry of nanostructured materials for energy applications, J. Electroceram. 1 (3) (1997) 239.
[2] M. Ferroni, M.C. Carotta, V. Guidi, G. Martinelli, F. Ronconi, M. Sacerdoti, E. Traversa, Preparation and characterization of nanosized titania sensing film, Sens. Actuators B-Chem. 77 (1,2) (2001) 163.
[3] S. Akrami, M. Watanabe, T.H. Ling, T. Ishihara, M. Arita, M. Fuji, K. Edalati, High-pressure TiO2-II polymorph as an active photocatalyst for CO_2 to CO conversion, Appl. Catal. B: Environ. 298 (2021) 120566.
[4] Q. Wang, M. Watanabe, K. Edalati, Visible-light photocurrent in nanostructured high-pressure TiO_2-II (Columbite) phase, J. Phys. Chem. C 124 (25) (2020) 13930.
[5] A. Verchère, S. Pailhès, S.L. Floch, S. Cottrino, R. Debord, G. Fantozzi, S. Misra, C. Candolfi, B. Lenoir, et al., Optimum in the thermoelectric efficiency of nanostructured Nb-doped TiO2 ceramics: from polarons to Nb–Nb dimers, Phys. Chem. Chem. Phys. 22 (23) (2020) 13008.
[6] C.P. Li, J.F. Wang, W.B. Su, H.C. Chen, Y.J. Wang, D.X. Zhuang, Effect of sinter temperature on the electrical properties of TiO2-based capacitor–varistors, Mater. Lett. 57 (8) (2003) 1400.
[7] C. Demetry, X. Shi, Grain size-dependent electrical properties of rutile (TiO2), Solid State Ion. 118 (3) (1999) 271.
[8] Y.I. Lee, J.-H. Lee, S.-H. Hong, D.-Y. Kim, Preparation of nanostructured TiO2 ceramics by spark plasma sintering, Mater. Res. Bull. 38 (6) (2003) 925.
[9] S.C. Liao, Y.J. Chen, W.E. Mayo, B.H. Kear, Transformation-assisted consolidation of bulk nanocrystalline TiO2, Nanostruct. Mater. 11 (4) (1999) 553.
[10] B. Ratzker, A. Wagner, M. Sokol, S. Kalabukhov, M.P. Dariel, N. Frage, Optical and mechanical properties of transparent alumina fabricated by high-pressure spark plasma sintering, J. Eur. Ceram. Soc. 39 (8) (2019) 2712.
[11] U. Anselmi-Tamburini, J.E. Garay, Z.A. Munir, Fast low-temperature consolidation of bulk nanometric ceramic materials, Scr. Mater. 54 (5) (2006) 823.
[12] F. Balima, F. Bellin, D. Michau, O. Viraphong, A. Poulon-Quintin, U.-C. Chung, A. Dourfaye, A. Largeteau, High pressure pulsed electric current activated equipment (HP-SPS) for material processing, Mater. Des. 139 (2018) 541.
[13] A. Knaislová, P. Novák, S. Cygan, L. Jaworska, M. Cabibbo, High-pressure spark plasma sintering (HP SPS): a promising and reliable method for preparing Ti–Al–Si alloys, Materials 10 (5) (2017) 465 (5).
[14] Y.L. Godec, S.L. Floch, S. Pailhes, J.-M. Combes, Device for sintering by pulsating current and associated method, US11247267B2, 2022.
[15] A. Verchère, S. Cottrino, G. Fantozzi, S. Mishra, T. Gaudisson, N. Blanchard, S. Pailhès, S. Daniele, S. Le Floch, Effect of high pressure spark plasma sintering on the densification of a Nb-doped TiO2 nanopowder, Ceramics 3 (4) (2020) 507 (4).
[16] Z.Z. Fang, H. Wang, V. Kumar, Coarsening, densification, and grain growth during sintering of nano-sized powders–a perspective, Int. J. Refract. Met. Hard Mater. 62 (2017) 110.
[17] B. Ratzker, A. Wagner, S. Kalabukhov, S. Samuha, N. Frage, Non-uniform microstructure evolution in transparent alumina during dwell stage of high-pressure spark plasma sintering, Acta Mater. 199 (2020) 469.
[18] Y. Le Godec, M.T. Dove, D.J. Francis, S.C. Kohn, W.G. Marshall, A.R. Pawley, G.D. Price, S.A.T. Redfern, N. Rhodes, et al., Neutron diffraction at simultaneous high temperatures and pressures, with measurement of temperature by neutron radiography, Mineral. Mag. 65 (6) (2001) 737.
[19] A.P. Hammersley, S.O. Svensson, M. Hanfland, A.N. Fitch, D. Hausermann, Two-dimensional detector software: from real detector to idealised image or two-theta scan, High Press. Res. 14 (4–6) (1996) 235.
[20] V. Guidi, M.C. Carotta, M. Ferroni, G. Martinelli, M. Sacerdoti, Effect of dopants on grain coalescence and oxygen mobility in nanostructured titania anatase and rutile, J. Phys. Chem. B 107 (1) (2003) 120.
[21] D.A.H. Hanaor, C.C. Sorrell, Review of the anatase to rutile phase transformation, J. Mater. Sci. 46 (4) (2011) 855.
[22] H. Zhang, J.F. Banfield, New kinetic model for the nanocrystalline anatase-to-rutile transformation revealing rate dependence on number of particles, Am. Mineral. 84 (4) (1999) 528.
[23] D. Machon, M. Daniel, V. Pischedda, S. Daniele, P. Bouvier, S. Le Floch, Pressure-induced polyamorphism in TiO2 nanoparticles, Phys. Rev. B 82 (14) (2010) 140102.
[24] D. Machon, M. Daniel, P. Bouvier, S. Daniele, S. Le Floch, P. Melinon, V. Pischedda, Interface energy impact on phase transitions: the case of TiO2 nanoparticles, J. Phys. Chem. C 115 (45) (2011) 22286.
[25] R.A. Roca, E.R. Leite, E. Longo, Compacting and densification of TiO2 nanoparticles, Process. Appl. Ceram. 11 (2) (2017) 93.
[26] X. Xue, X. Luo, Y. Long, L. Zhang, Y. Yin, B. Xu, Kinetic study on the effect of iron on the grain growth of rutile-type TiO_2 under in situ conditions, Mater. Res. Express 9 (5) (2022) 055008.
[27] F. Maglia, M. Dapiaggi, I.G. Tredici, U. Anselmi-Tannburini, Synthesis of fully dense anatase TiO2 through high pressure field assisted rapid, Nanosci. Nanotechnol. Lett. 4 (2) (2012) 205.
[28] S.C. Liao, W.E. Mayo, K.D. Pae, Theory of high pressure/low temperature sintering of bulk nanocrystalline TiO2, Acta Mater. 45 (10) (1997) 4027.
[29] S.C. Liao, K.D. Pae, W.E. Mayo, Retention of nanoscale grain size in bulk sintered materials via a pressure-induced phase transformation, Nanostruct. Mater. 8 (6) (1997) 645.
[30] S. Grasso, B.-N. Kim, C. Hu, G. Maizza, Y. Sakka, Highly transparent pure alumina fabricated by high-pressure spark plasma sintering, J. Am. Ceram. Soc. 93 (9) (2010) 2460.
[31] M. Sokol, M. Halabi, S. Kalabukhov, N. Frage, Nano-structured MgAl2O4 spinel consolidated by high pressure spark plasma sintering (HPSPS), J. Eur. Ceram. Soc. 37 (2) (2017) 755.
[32] J.-P. Maria, X. Kang, R.D. Floyd, E.C. Dickey, H. Guo, J. Guo, A. Baker, S. Funihashi, C.A. Randall, Cold sintering: current status and prospects, J. Mater. Res. 32 (17) (2017) 3205.
[33] Q. Jin, L. Zhao, X. Zhang, R. Zhang, B. Cui, Densification and fine-grain formation mechanisms of BaTiO3 ceramics consolidated by self-assembly sintering, J. Mater. Sci: Mater. Electron. 32 (6) (2021) 8043.
[34] M. Rossetti, G. da, S. Falk, A.N. Klein, S.Y. Gómez González, C. Binder, D. Hotza, Plasma-assisted rapid sintering of nanotitania powders, J. Eur. Ceram. Soc. 42 (4) (2022) 1670.
[35] R. Coble, Sintering crystalline solids. 1. Intermediate and final state diffusion models, J. Appl. Phys. 32 (5) (1961) 787.
[36] A. Weibel, R. Bouchet, P. Bouvier, P. Knauth, Hot compaction of nanocrystalline TiO2 (anatase) ceramics. Mechanisms of densification: grain size and doping effects, Acta Mater. 5 (13) (2006) 3575 (13).
[37] L. Balice, M. Cologna, F. Audubert, J.-L. Hazemann, Densification mechanisms of UO2 consolidated by spark plasma sintering, J. Eur. Ceram. Soc. 41 (1) (2021) 719.
[38] I. Issa, L. Joly-Pottuz, J. Rethore, C. Esnouf, T. Douillard, V. Garnier, J. Chevalier, S. Le Floch, D. Machon, et al., Room temperature plasticity and phase transformation of nanometer-sized transition alumina nanoparticles under pressure, Acta Mater. 150 (2018) 308.
[39] E. Calvié, J. Réthoré, L. Joly-Pottuz, S. Meille, J. Chevalier, V. Garnier, Y. Jorand, C. Esnouf, T. Epicier, et al., Mechanical behavior law of ceramic nanoparticles from transmission electron microscopy in situ nano-compression tests, Mater. Lett. 119 (2014) 107.
[40] M.J. Mayo, High and low temperature superplasticity in nanocrystalline materials, Nanostruct. Mater. 9 (1) (1997) 717.
[41] R. Chaim, M. Levin, A. Shlayer, C. Estournes, Sintering and densification of nanocrystalline ceramic oxide powders: a review, Adv. Appl. Ceram. 107 (3) (2008) 159.
[42] J. Rankin, L.A. Boatner, Unstable neck formation during initial-stage sintering, J. Am. Ceram. Soc. 77 (8) (1994) 1987.
[43] F. Balima, V. Pischedda, S. Le Floch, A. Brulet, P. Lindner, L. Duclaux, A. San-Miguel, An in situ small angle neutron scattering study of expanded graphite under a uniaxial stress, Carbon 57 (2013) 460.
[44] B. Ratzker, A. Wagner, M. Sokol, S. Kalabukhov, N. Frage, Stress-enhanced dynamic grain growth during high-pressure spark plasma sintering of alumina, Acta Mater. 164 (2019) 390.
[45] J. Guignard, M. Prakasam, A. Largeteau, High pressure (HP) in spark plasma sintering (SPS) processes: application to the polycrystalline diamond, Materials 15 (14) (2022) 4804 (14).